Statistical Study of the Non-thermal Continuum Radiation Beaming Angle measured by the High Frequency Receiver on Van Allen Probes-A

S. A. Boardsen[1,2], E.-H. Kim[3], J. L. Green[4], C. Z. Cheng[3], I. H. Cairns[5], J. R. Johnson[6]

[1]NASA Goddard Space Flight Center, Greenbelt, Maryland, USA.

[2]Goddard Planetary Heliophysics Institute, University of Maryland in Baltimore, Maryland, USA.

[3]Princeton Plasma Physics Laboratory, Princeton University, Princeton, New Jersey, USA

[4]Space Science Endeavors LLC, Silver Spring, Maryland, USA

[5]Department of Physics, University of Sydney, Sydney, New South Wales, Australia

[6]Department of Engineering, Andrews University, Berrien Springs, Michigan, USA

Corresponding author: S. A. Boardsen (scott.a.boardsen@nasa.gov)

Key Points: (140 characters or less with no special characters or acronyms)

- Nonthermal continuum radiation beaming angles are calculated over the entire seven-year mission of Van Allen Probes-A.

- For frequencies $\lesssim$100 kHz the observed beaming angle pattern is consistent with the predictions from Linear Mode Conversion Theory.
- For frequencies $\gtrsim$100 kHz another mechanism along with Linear Mode Conversion is needed.

Keywords: Linear Mode Conversion Theory, Nonthermal Continuum Radiation, Terrestrial Myriametric Radiation

Abstract

The nonthermal continuum radiation (NTC) beaming angle is computed over the entire Van Allen Probes A mission when the spacecraft was in the dawn sector. The conditions in the dawn sector are favorable for the wave vector to lie near/in the spacecraft's spin plan allowing a favorable estimate of the beaming angle, and the dawn sector is also advantageous in that previous studies show NTC occurrence to peak in this sector. We found that scatter plots, over the entire mission, of beaming angle versus magnetic latitude form a distinct inverted V pattern, with the apex at/near the magnetic equator. This pattern was sharpest for frequencies (f) $\lesssim$ 100 kHz. Using the NTC beaming formula from LMCT, we show that such an inverted V pattern is expected due to the large variation in the plasmapause location over the entire mission. The theoretical derived pattern qualitatively reproduces the observed pattern but not quantitatively. The lack of quantitative agreement is discussed and is attributed to several factors, one factor is off centered emissions from the radio window. The qualitative agreement strongly supports LMCT as being the dominant mechanism generating NTC for $f \lesssim$ 100 kHz. For $f \gtrsim$ 100 kHz the inverted V pattern becomes less distinct, and strong near equatorial beaming is observed. After considering contamination of our selections by left-handed polarized AKR, our study suggests that besides LMCT another unidentified NTC generation mechanism becomes important for $f \gtrsim$ 100 kHz.

Plain Language Summary

No summary given. Not required.

1. Introduction

Non-thermal continuum (NTC) radiation (also called terrestrial myriametric radiation) is free space ($f > f_{pe}$, f_{ce}, where f, f_{ce}, and f_{pe} are the wave, electron cyclotron, and plasma frequencies respectively) electromagnetic (EM) radiation for waves in the left-handed ordinary (L-O) mode observed in and near the Earth's magnetosphere and mainly outside the plasmasphere (Gurnett & Shaw, 1973; Gurnett 1975). NTC is believed to be emitted at strong density gradients chiefly at the equatorial plasmapause and is associated with electrostatic (ES) waves near the upper hybrid frequency (Gough et al., 1979; Kurth et al., 1981) and electron injections (Gough, 1982). This radiation can be produced over a broad frequency range from ~10 kHz to 100's of kHz and is roughly divided into two categories 1) trapped continuum where $f < f_{pe}$ at the magnetopause and escaping continuum where $f > f_{pe}$ at the magnetopause (Kurth et al., 1981). For $f \gtrsim 100$ kHz, escaping radiation is often called kilometric continuum (KC) radiation (Hashimoto et al., 1999; Green et al., 2002; Green et al., 2004; Hashimoto et al., 2005).

The widely accepted theory for the generation of NTC is linear mode conversion theory (LMCT) (Jones, 1976; Budden, 1980, Horne et al., 1989). In this theory electrostatic waves (ES) at frequencies of $\sim(n+½)\, f_{ce}$ (Kurth et al., 1979) are generated by electron loss cone distributions (Gough et al., 1979; Rönnmark & Christiansen, 1981) or weak ring-like features in the electron distribution (Sentman et al., 1979; Kurth et al., 1980) at/near the magnetic equator. As these ES waves propagate toward the higher density plasmapause, they convert into electromagnetic (EM) Z-mode waves on the same dispersion branch (e.g., Oya, 1971). Mode conversion from incoming Z-mode to the free space L-O wave mode radiation occurs at the radio window, where the Z-

mode frequency matches the local electron plasma frequency. This process is depicted in Figure 4 of Jones (1980) and Figure 8 of Horne et al. (1989).

The key prediction of LMCT by Jones (1976) is that the mode-converted L-O mode waves can form two symmetrical beams relative to the magnetic equator as they propagate away from the equatorial plasmapause into lower densities outside the plasmasphere. The LMCT beaming formula is

$$\theta_B = \tan^{-1}\sqrt{\frac{f_{pe\_w}}{f_{ce\_w}}}. \quad (1)$$

Here, θ_B is the beaming angle measured from the background magnetic field at the radio window ***B*** (***k*** || +***B***) or -***B*** (***k*** || - ***B***), ***k*** is a wave vector, f_{pe_w} and f_{ce_w} are the electron plasma and cyclotron frequencies at the window, respectively, and at the radio window, $f = f_{pe\_w}$ (Jones, 1980). The beaming formula holds at the window center where the waves experience no attenuation upon crossing. The window center is where the incoming Z-mode ***k*** is either parallel or anti-parallel to ***B***. Therefore, if Z-mode waves are propagating into the window from both the +***B*** and -***B*** directions, two symmetric L-O mode free space beams about the magnetic equator will be emitted from the radio window. We note that θ_B is the predicted asymptotic refraction (propagating away from the radio window as the index of refraction →1) of ***k*** away from the ***B*** direction as it propagates into the lower plasma density. For a typical plasmapause density gradient, this refraction of ***k*** from θ of 0° at the radio window center to ~ θ_B will occur over a radial distance of less than ~0.1 R_E, where R_E is Earth's radii (Jones, 1980; Horne, 1989). For off centered emission's the wave attenuation increases as the deviation of the beaming angle away

from θ_B increases (Budden, 1980). We note that studies often use the complement of θ_B; $\lambda_B = \tan^{-1}(\sqrt{(f_{ce\_w} / f_{pe\_w})})$, which is a beaming angle between $\boldsymbol{k}$ and the magnetic equatorial plane.

The acceptance of the LMCT theory is based primarily on Jones et al. (1987), where Dynamics Explorer-1 observed two symmetrical NTC beams in magnetic latitude (λ_M) as the spacecraft transverses the magnetic equator. Other follow-up studies seeking to further verify the LMCT interpretation have either negative or mixed results (Morgan & Gurnett, 1991; Grimald et al., 2007) on the beaming angle predictions. Two multi-event/case studies of KC using GEOTAIL (Hashimoto et al., 2005) and IMAGE (Boardsen et al., 2008) spacecraft concluded that the LMCT beaming formula predicted too small (too large if complement of beam angle is used instead) of a beam angle θ_B compared to the λ_M where the KC was observed.

In this paper, using the Van Allen Probes-A High Frequency Receiver (HFR) dataset over the entire mission, we perform a statistical study of the observed beaming angle θ_B as a function of the spacecraft position and compare it with that predicted by LMCT. This paper is organized as follows. Section 2 describes the dataset and how θ_B is computed. Section 3 explores the statistical set of θ_B observations. Section 4 derives the theoretically predicted beaming angle using equation (1) as a function of satellite location, followed by a discussion and conclusion.

2. Remote Measurement of the Observed Beaming Angle

For observational studies cited in the introduction and this study, the electromagnetic radiation in the NTC frequency range was only sampled by one spin plane electric field antenna.

Therefore, the only approach to estimate the wave vector direction and the source beaming angle is from the analysis of the antenna's spin modulation curve. The modulation curve is (e.g., Kurth et al., 1975)

$$\left(\frac{E_i}{E_0}\right)^2 = \left(1 - \frac{m}{2}\right) - \frac{m}{2}\cos[2(\delta_i - \delta)], \qquad (2)$$

where E_i is the component of the vector electric field $\boldsymbol{E}$ measured by the spacecraft antenna at time step i, E_0 is the peak spin plane electric field, m is the modulation index, δ is the azimuthal angle of k in the spin plane, and δ_i is the antenna angle in the spin plane. At the time of the null ($\delta_i = \delta$) the antenna is aligned with the projection of $\boldsymbol{k}$ onto the spin plane because $\boldsymbol{k} \bullet \boldsymbol{E}=0$ for free space radiation. The modulation index m=1 corresponds to full modulation ($\boldsymbol{k}$ lies in the spin plane) and m =0 corresponds to no modulation.

In this study, we use the High Frequency Receiver (HFR) on the Van Allen Probes A spacecraft (Kletzing et al., 2013) for which only one spin plane electric field antenna is sampled by the receiver for a given time interval. Because we want $\boldsymbol{k}$ to lie nearly in the spin plane to estimate θ_B, we need to analyze time intervals where the spin axis direction is nearly perpendicular to the radial direction of the Earth. The Van Allen Probes spin axis vector, which points to within ±28° of the Sun, is nearly perpendicular to the radial direction for MLTs around 6 MLT and 18 MLT. Continuum typically peaks around dawn (Gurnett and Frank, 1976). Fits were made only for periods when the angle between the spin axis and the radial position vector (Earth centered) was within $\pm 15^o$ of perpendicular orientation. In all, 6408 dawn sector time intervals were processed from 2012/10/15 to 2019/06/20. The onboard HFR spectral

measurements consist of 82 logarithmically spaced frequencies ranging from 10 to 487 kHz. The cadence of the frequency sweeps is 0.5 s, which is small compared to the spin period of ~11 s. For each dawn sector time interval, spin modulation curve fits were performed on the HFR spectra dataset (Kletzing et al., 2022). Fits were performed for each frequency over a time range covering 1&1/2 spin periods (~33 measurements, ~17 s), staggering each time step by the one-time measurement between individual fits.

The analysis approach used in this study is that described in Morgan and Gurnett (1991). We rewrite the modulation equation (2) as

$$\rho_i(f) = \mathrm{C}_1 + \mathrm{C}_2 \cos(2\delta_i) + \mathrm{C}_3 \sin(2\delta_i) \quad (3)$$

where $\rho_i(f)$ is the measured electric field power spectral density at frequency *f*, δ_i is and antenna spin phase angle at time step *i*, respectively, and C_1, C_2, and C_3 are the fit coefficients. Least squares fit of equation (3) are made over all data points within ±¾ of a spin period about the time of the center point *i*, solving for the fit coefficients C_1, C_2, and C_3. A five-point smoothing is performed on $\rho_i(f)$before fitting. The uncertainties of the fit coefficients ΔC_1, ΔC_2, and ΔC_3 are computed from the product of their variance with the diagonal elements of the covariance matrix (Bevington & Robinson, 1992). We found that the off-diagonal elements of this matrix are small relative to the diagonal elements, so the cross-correlations are set to zero when estimating the uncertainties in *m*, δ, and λ_0.

From C_1, C_2, C_3, ΔC_1, ΔC_2, and ΔC_3, one can compute *m*, δ, λ_0, and their uncertainties Δm, $\Delta\delta$, $\Delta\lambda_0$ as

$$m = 2\sqrt{C_2{}^2 + C_3{}^2}/(C_1 + \sqrt{C_2{}^2 + C_3{}^2}), \quad (4)$$

$$\delta = \frac{1}{2}\tan^{-1}(C_3/C_2), \quad (5)$$

$$\cos^2(\lambda_0) = m. \quad (6)$$

In equation (6) λ_0 is the angle of $\boldsymbol{k}$ out of the spin plane. The uncertainties Δm, $\Delta\delta$, $\Delta\lambda_0$ are computed from square root of the square of differential form of equations (4-6) and setting the terms involving $\Delta C_1 \Delta C_2$, $\Delta C_2 \Delta C_3$, and $\Delta C_3 \Delta C_1$, to zero due to their small cross-correlations. We note that Fainberg (1979) uses a different representation of the modulation curve $\left(\frac{E_i}{E_1}\right)^2 = 1 - m' \cos[2(\delta_i - \delta)]$, where E_1 is a constant and $0 \leq m' \leq 1$ is the modulation index, compared to equation (1) of this paper. The relation between the modulation index's is $m' = \frac{m}{2-m}$, λ_0 would be given by $cos^2(\lambda_0) = \frac{2m'}{1+m'}$. Both approaches are equally valid. The representation by Fainberg (1979) was used by Menietti et al. (1998) to estimate the direction of Jovian radio emissions.

Figure 1 is an example spin fit of the modulation curve for the frequency channel at 38.3 kHz. The fit parameters and their uncertainties are listed in the figure. For this fit, the uncertainty in δ is 3.6°, in 0.5 s between spectral measurements the antenna rotates through angle of ~16°. Using the spacecraft ephemeris (see Data Availability Statement) and the NAIF SPICE toolkit (Acton, 1996; Acton et al. 2017), the antenna orientation at the time of the null in modulation curve indicated by the blue curve in Figure 1 was computed. The antenna's unit vectors are in Solar Magnetic (SM) coordinates ($\boldsymbol{u}$, $\boldsymbol{v}$, $\boldsymbol{w}$), where $\boldsymbol{u}$ and $\boldsymbol{v}$ are in the spin plane, and $\boldsymbol{w}$ is along

182 the spin axis. For SM coordinates, the origin is Earth centered and the Z-axis (Z_{SM}) is parallel to
183 the north magnetic pole. If the HFR is connected to ***u*** (or ***v***) antenna, then projection of
184 wavevector ***k*** into the spin plane ($\widehat{\boldsymbol{k}}_{sp}$) is aligned with ***u*** (or ***v***) to within a sign. The sign is
185 chosen such that -***k*** points Earthward (directed nearest to the Z_{SM} axis). The beaming angle Θ_B is
186 estimated as an angle between $\widehat{\boldsymbol{k}}_{sp}$ and $\boldsymbol{Z}_{\mathrm{SM}}$ if the spacecraft is in the northern hemisphere, and
187 $\widehat{\boldsymbol{k}}_{sp}$ and the -$\boldsymbol{Z}_{\mathrm{SM}}$ axis if the spacecraft is in the southern hemisphere.
188
189 We retain only Θ_B measurements for which a plasma density measurement (Kurth et al.,
190 2015) was available in the plasma density data set (Kurth et al., 2020) for each fit time interval.
191 The local plasma density is needed to compute the local plasma frequency f_{pe} to restrict the
192 frequencies to the free space mode.
193
194 The 6408 processed time intervals were filtered for NTC emissions with strong
195 modulation using the following criteria: $f > 1.2f_{\mathrm{pe}}$, $m>0.6$, $\Delta m/m < 0.2$, $\chi^2/\chi_0^2<0.25$. We use
196 χ^2/χ_0^2 <0.25 in order that the sinusoidal fit is substantially improved over the constant offset fit
197 given by χ_0^2. We also removed data during intervals judged to be saturated, this removed about
198 4% of the data points. Applying this filter reduces our set of Θ_B measurements to 1.6×10^7
199 frequency-time pixels. We found that the modulation index of type III radio bursts was
200 consistently < 0.4, so contamination of our selections by these radio bursts is minimal.
201
202 Smoothing the signal will lower the modulation index because the dc component of the
203 signal will not change, while the ac component will become smaller in amplitude. If the signal is

a sine curve, the effect on *m* due to smoothing can be computed. The amplitude of a smoothed sine curve of unit amplitude is given by

$$b(\alpha, n) = \left(1 + 2\sin(n\alpha)\cos\left((n+1)\alpha\right) / \sin(\alpha)\right)/(2n+1), \quad (7)$$

where 2n+1 is the amount of smoothing, and α is the angular increment between measurements. For five-point smoothing $n = 2$ and from the antenna rotation angle between measurements $\alpha = 2{\cdot}16°$, $b(\alpha, n) = 0.715$. The relation between *m* from the smooth sine curve and the modulation index m_c from the non-smoothed sine curve is

$$m_c = 2m/(2b(\alpha, n) + m\left(1 - b(\alpha, n)\right). \quad (8)$$

The value $m = 0.6$ used as the lower limit in filtering the data gives $m_c = 0.750$, which from equation (6) gives an out of spin plane angle estimate limit of 30° for the wave vector.

Frequency-time spectrograms of two orbital segments where the spin modulation curves were fitted are shown in Figures 2 and 3 for (a) spectral power density, (b) the modulation index *m*, (c) the chi-squared ratios χ^2/χ_0^2 and (d) selections that satisfied the selection criteria. The red line in Figure 3d at 53.6 kHz between 4.5 and 5 R_E are data points used in Figures 8, 9, &10. For $f > 100$ kHz strong contamination of the selections can occur. Figure 5 shows an extreme example of selected emissions $200 < f < 500$ kHz interpreted to be heavily contaminated by L-O mode AKR when the spacecraft is at $\lambda_M > 10°$ and $R > 5.3\ R_E$ in dawn sector (MLT ~ 6). Green et al. (1977) using ray tracing showed that L-O mode can propagate from the source (dusk sector

auroral field lines) across the polar cap and down to λ_M of about 10° on the dawn sector (unlike R-X mode AKR (Green et al., 1977; Xiao et al., 2016) which can easily propagate to the dusk sector equatorial inner magnetosphere). Looking at the ray tracing results of Green et al. (1977) this contamination will decrease as the magnetic latitude decreases in the dawn sector.

Histograms of the selected frequency-time pixels are presented in Figure 4 of (a) the radial distance (R), (b) the magnetic local time (MLT), (c) λ_M for f < 100 kHz, and (d) λ_M for f > 100 kHz. The y-axis is the number of selected frequency-time pixels per bin. Splitting the frequencies into those below and those above 100 kHz is because the emissions show a distinct change in the spatial characteristics as discussed in the next section. The magnetic latitude histograms are substantially different between f < 100 kHz (Figure 4(b)) and f > 100 kHz (Figure 4(d)). While the lower frequency case (f < 100kHz) shows a deep minimum at the magnetic equator, the higher frequency case (f > 100kHz) shows a strong peak at the magnetic equator. The former f < 100 kHz is quantitatively consistent with LMCT in the sense that the beaming is predicted to be directed out of the equatorial plane, while the later f > 100 kHz is not consistent with LMCT and is more consistent with the findings of Hashimoto et al. (2005) and Boardsen et al. (2008) where stronger equatorial beaming was suggested than that predicted by LMCT. The counts pick up moving away from the magnetic equator for f > 100 kHz in Figure 4(d), and we interpret this to be due to contamination of selections by L-O mode AKR which is predicted to become stronger as λ_M increases (Green et al. 1977).

3. Observed Beaming Angles Versus Magnetic Latitude

We explored scatter plots of the selections for each frequency as a function of various parameters against beaming angle (e.g., like radial distance, magnetic latitude, etc.). For scatter plots of magnetic latitude, the scatter exhibited an inverted V pattern with the apex at/near the magnetic, with the pattern clearer for frequencies below 100 kHz. Figure 5 shows scatter plots of θ_B versus λ_M when spacecraft is located at a radial distance between 4 and 5 R_E ($4R_E < r < 5R_E$) for various frequency ranges, for a) $f > 19$ and < 51 kHz and b) $f > 51$ kHz and $f < 100$ kHz, c) $f >$ 100 kHz and $f < 147$ kHz, and d) $f >$147 kHz and $f < 500$ kHz. Beyond the division at 100 kHz, the choice of frequency boundaries is arbitrary. For Figure 5(a-b), a distinct statistical inverted V pattern is observed about the magnetic equator. Note that the gap in detections in Figure 5(a) is consistent with the notch in the histogram in Figure 4(a). For Figure 5(c-d), an inverted V signature for $|\lambda_M| < 10°$ is observed in the running median, while for $|\lambda_M| > 10°$ we interpret the scatter to be strongly contaminated by L-O mode AKR.

Scatter plots of θ_B versus MLAT for 5.5 $R_E < r < 6$ R_E are shown in Figure 6(a-d). For the lower frequency radiations ($f <$ 100kHz), an inverted V pattern is observed about the magnetic equator as shown in Figure 6(a-b), while no inverted V pattern is discernable for the higher frequencies as shown in Figure 6(b, d), which is interpreted to be due to L-O mode AKR contamination. Can the inverted V structure of beaming angles versus magnetic latitude observed in scatter plots covering the entire seven-year mission be explained in terms on LMCT? This will be explored in the next section.

4. Model Beaming Angle versus Spacecraft Position for Varying Plasmapause Location

If LMCT is the principal generation mechanism, what is the predicted statistical θ_B pattern as a function of spacecraft position and detected NTC frequency f for a wide range of plasmapause locations? Figure 7(a) illustrates the meridian geometry used to interpret the results of our observational data analysis. The following assumptions are used: background magnetic field is an Earth center dipole anti-aligned with the Z_{SM} axis; the radio window is located at the equatorial plasmapause; the plasmapause is assumed to have local azimuthal symmetry; the emission is from the center of the window. Under these assumptions, the ray lies in the meridian plane. In Figure 7(a), the radio window (*W*) is located at an equatorial plasmapause at $2.5R_E$, the blue line is the emitted NTC ray path for $f = f_{pe\_w}$ from *W* to the spacecraft (*SC*). Knowing the location of the radio window and spacecraft the beaming angle can be computed as

$$\tan\theta_B = \frac{\rho_{sc}-\rho_w}{z_{sc}}. \quad (9)$$

The *SC* and *W* locations in the ρ -z plane is given by (ρ_{sc}, z_{sc}) and $(\rho_w, 0)$ respectively, where $\rho = \sqrt{x^2 + y^2}$ in units of R_E. Using an Earth centered magnetic dipole f_{ce_w} is given as

$$f_{ce\_w} = \frac{870}{{\rho_w}^3} \text{ Hz} \quad (10)$$

for a dipole moment of $3.11\text{x}10^{-5}$ T. For this example, from the *SC* and *W* location $\theta_B = 47.9°$ from equation (9) and from equation (1&10) $f = f_{pe\_w} = 68.1$ kHz. For variable *W* location in equatorial radius (Figure 7b) and fixed f and SC r the solution of equations (1&9&10) results in an inverted V pattern for θ_B versus λ_M (Figure 7c).

Figure 7(b) shows how θ_B varies for different source locations W in the equatorial radial distance for four different NTC waves of f = 33.2, 53.6, 68.1, and 121.0 kHz. For example, for a sharp plasmapause at 2.5R_E, θ_B is equal to 37.7°, 44.4°, 47.9° and 55.7° for the four frequencies, indicated by the black dots in Figure 7(b) and the latitudes at which the *SC* will observe them in Figure 7(c). The increase in θ_B with increasing ρ_{SM} in Figure 7(b) is due to the increasing f_{pe_w}/f_{ce_w} ratio with increasing ρ_{SM} for fixed f_{pe_w}. Thus, as the magnetosphere becomes less active the geomagnetic K_p index decreases and the plasmapause moves outwards (e.g., Carpenter & Anderson, 1992; Moldwin et al., 2002) and θ_B will increase.

Figure 7(c) presents the predicted model θ_B for an SC radial position at 4.75 R_E as a function of magnetic latitude λ_M for plasmapause locations varying between 1.5 to 4.75 R_E. For a sharp plasmapause at 2.5R_E, the frequencies emitted at W (black dots in Figure 7(b) will be detected by the *SC* with a radial position R_{SC} = 4.75R_E at λ_M = ± 27.7°, ± 23.5°, ± 21.5°, and ± 17.0° (black dots in Figure 7c) for these four f respectively. For fixed radial position R_{SC} of the SC, as the plasmapause location varies due to changing geomagnetic conditions, an inverted V pattern of θ_B versus λ_M with the apex located at the magnetic equator will be traced out as shown in Figure 7(c). The source location coincides with the virtual spacecraft position at the apex of the inverted V at $\lambda_M \rightarrow 0°$. As noted, because the beaming formula is asymptotic θ_B does not equal the Z-mode angle of 0° at the radio window center.

Figure 8 shows a comparison of the observations with the model of Figure 7, for the same f and SC radial distances that lie within $4.5 < r < 5\ R_E$. A scatter plot of θ_B versus λ_M is shown in Figures 8(a-d) for these four f. The error bars for θ_B are plotted for 10 randomly selected points. To restrict the wave vector to lie closer to the spin plane, only points are plotted for which $m >$

0.8 (m_c = 0.96). The three blue curves are the theory curves for SC positions at r of 4.5, 4.75, and 5 R_E. Comparing the observations with the blue theory curves, one can see that the observations are qualitatively consistent with the model but are not always quantitatively consistent. With the disagreement of observed θ_B with model the largest around λ_M of 0°, with the observations about 10° larger than the model θ_B. Why quantitative agreement within measurement error is difficult and maybe impossible to obtain is discussed in the next section.

For f = 33.2, 53.6, 68.1 kHz a gap in the observations is observed straddling λ_M of 0° which would be expected from the off-equatorial beaming predicted by the theory. No such gap is observed for the large clustering of points for f = 120 kHz which is not consistent with the theory.

Can we detect a K_p dependence related to changing plasmapause location over the entire mission mentioned earlier in this section? Figure 8(e-h) plots K_p (Papitashvili and King, 2020) versus λ_M for the selections of Figure 8(a-d). The red lines are linear fits for $1 \leq K_p \leq 4$, and the number in each panel is the Spearman correlation coefficient. Unlike the linear fit, which is just a visual aid, this correlation is a nonlinear correlation which measures the degree that the data is monotonically related, a value of 1 indicates a strict monotonic increasing dependence, while a value of -1 indicates a strict monotonic decreasing dependence. The negative sign of the coefficients is consistent with the expected change in plasmapause position with θ_B. However, the correlation is weak for f = 33.2 kHz with a value of -0.29, moderate for f = 53.6 and 68.1 kHz with values of -0.43 and -0.51 respectively, and for f = 120 kHz the value of -0.21 is poor. So below 100 kHz the correlation is moderate at best. We note that in the study of Moldwin et al.

(2002) the non-linear correlation for the overall dataset of radial plasmapause position versus K_p is 0.55 (see Figure 4 of that study), we should not expect to get a better correlation than this value since K_p is a fuzzy indicator of the plasmapause location. The uncertainty in the measurement of θ_B will also degrade the correlation.

5. Discussion

Qualitatively the observations for $f < 100$ kHz reproduce the inverted V structure of θ_B vs. λ_M predicted by LMCT theory for the large variation in plasmapause location over the duration of the mission. However, the error bars of many measurements do not encompass the model curve, with a systematic bias, especially for observations near the magnetic equator. We discuss why one might not expect quantitative agreement. Three major simplifications are used in our analysis: 1) the dawn sector plasmapause in our model is azimuthally symmetric, it has no azimuthal dependence. This allows one to use the simple model shown in Figure 7 for comparison with data. 2) The out of spin plane component is not used in the computation of θ_B, we justify this by using only data points with a large modulation index $m > 0.6$. 3) The emissions not from the center of the radio window need to be considered.

A radially directed plasmapause gradient used in this study is obviously an approximation. There are azimuthal variations in the plasmapause location as observed by the Extreme Ultraviolet Imager on the IMAGE spacecraft (e.g., Sandel et al., 2003). Here we make a back of the envelope estimate of how this could lead to a systematic offset of about 10°. To simplify the argument the measurement of azimuthal angles in SM coordinate system is shifted

to the SC location. From Section 2, the lower limit used in the filter for the modulation index is m=0.8 (m_c = 0.96) which after correcting for smoothing gives a maximum out of plane angle for $\boldsymbol{k}$ of about 10.7°. Combining this angle with the requirement that the analyzed data segments are within ±15° of being radially directed gives an azimuthal angular range of ±26°. So, if the source is not radially outwards, but directed 26° in azimuth from the radial direction, the radial location of the azimuthally directed radio window of the source can be estimated. If the spacecraft is near the equator at a radial distance is 4.75 R_E and the plasmapause is 2.5 R_E (for a radially directed outward beam), using the law of cosines a radial distance of about 2.7 R_E for the radio window is computed for the azimuthally directed beam. Looking at Figure 7(b) the model beaming angle for a window at 3 R_E is about 5 degrees larger than the beaming angle for a window at 2.5 R_E and this will lead to a systematic offset. We note that the magnitude of the systematic offset will diminish as the radially directed window moves outward in radius, because the slope of the curve in Figure 7(b) decreases with increasing radius.

In principle, the modulation index m can be used to estimate the out of spin plane component of the wave vector direction. However, there are several factors that limit the interpretation of m and, therefore, its use in computing the out of spin plane component. 1) One factor is the variation of Z-mode radiation at the source over the time interval ~17 s of the fit. For example, the detected NTC in Figure 1 is not sinusoidal, and this could be due to variation of the Z-mode radiation at the source. The deviation of the observations from a sinusoidal curve limits the interpretation of m. 2) The smoothing of the data will lower the estimate of m, but this can somewhat be overcome by using the estimated correction given by equation (8). 3) The presence

382 of background radiation can also degrade that interpretation of *m*, leading to a lowering of its
383 actual value.
384
385 Many observations of NTC are not emissions from near the window center where the
386 signal attenuation is near zero, but off centered where the signal experiences stronger
387 attenuation. We will address attenuation using the f=53.6 kHz emissions from the orbit segment
388 shown in Figure 2. The attenuation equation (23) of Budden (1980) will be used. This equation
389 requires as input f_{ce_w}, $f=f_{pe\_w}$, S_1, S_2 and G; where S_1 is the asymptotic direction cosine of the
390 emitted radiation along $\boldsymbol{B}$, S_2=0 is the direction cosine normal to both $\boldsymbol{B}$ and the density gradient,
391 here $\boldsymbol{B}$ is taken to be perpendicular to the density gradient, and the scalar of the density gradient
392 is G. To estimate the location of the window we will use the nearest plasmapause (Figure 9(a))
393 where f intersects f_{pe_w}, this occurs at 2016-07-12T18:37:06.482Z (red dots), where L=3.65, $|\lambda_M$
394 = 7.18°, MLT=7 h and f_{ce} = 18.34 kHz. Projecting this location using a dipole field line to the
395 magnetic equator gives f_{ce_w} =17.04 kHz. The density variation is assumed to be in a function of
396 only l-shell, and G is estimated to be -1971 m^{-4} from the gradient of the observed density
397 variation with l-shell (Figure 9(b)).
398
399 The radiation pattern from the radio window is shown in Figure 9(c), -10 dB corresponds
400 to a decade decrease the power spectral density. The window center is indicated by the black dot
401 where the attenuation is 0 dB (100% transmission) and ϕ is azimuthal angle measured from the
402 window location, a ϕ of 0° is directed outwards. We note that a spacecraft at ϕ of 30° will
403 detect a 3 decade drop relative to the window center in the power spectral density. Using
404 the same assumptions (ϕ =0°) as that used in Figure 7 for f=53.6 kHz, we show in Figure

405 9(d) that inverted V pattern persists as a function of dB for a plasmapause varying from 1.5
406 to 4.75 R_E. Including attenuation broadens the pattern in θ_B.
407

408 For the NTC beam at 53.6 kHz (Figure 2) the scatter plot of its observed θ_B versus time is
409 shown in Figure 10(a). The black curve is the beaming angle θ_{BC} computed from the orbital
410 position and the equatorial location of the plasmapause (Figure 9b). Based on the earlier
411 discussions it is not expected that the scatter plot of beaming angle and the beaming angle curve
412 should quantitatively agree, but they show similar trends with θ_B decreasing as the plasmapause
413 is approached. A scatter plot of its phase space density versus time is shown in Figure 10b. Using
414 θ_{BC} the attenuation (blue curve in Figure 10(b)) in dB on transmission through the radio window
415 is computed using the parameters given in Figure 9(c). The shape of this curve is like the trend in
416 the scatter; level near the window and decreasing moving toward larger radii, however the
417 decrease with power and distance from the window is not factored in. The solid (dashed) curve is
418 proportional to the product of the radio window attenuation times $1/\rho_w{}^2$ ($1/\rho_w$), $1/\rho_w{}^2$would be a
419 point source and $1/\rho_w$ would be a line source. Moving away from the plasmapause the power
420 spectral density decreases by 3 orders of magnitude. Both the dotted-dashed and dotted curves
421 drop off more rapidly than the observed scatter. This could be due to at least two factors 1) the
422 true plasmapause of the radio window location is further outwards in radius than that of the
423 proxy used (Figure 9b). 2) The power spectral density of the incoming Z mode does not peak at 0
424 or 180° but peaks at wave normal angles off 0 or 180 °, this would move the $1/\rho_w{}^2$ and $1/\rho_w$
425 curves to higher PSD moving outwards in radius. Figure 10(a, b) suggests that a significant
426 fraction of the observations are emissions that are off centered from the window center.

For NTC with f > 100 kHz another mechanism along with LMCT must be occurring. At least three studies have suggested mechanisms for the direct generation of KC. Farrell (2001) suggested that weak energetic electron beams in a dense warm plasma (where $f_{pe} >> f_{ce}$) can directly generate L-O emission with propagation nearly perpendicular. Cheng (1975) has proposed a mechanism that will lead to near perpendicular beaming using electron ring distributions as the source. Horky and Omura (2019) performed electromagnetic simulations with an electron ring beam source in a warm plasma with a density gradient and suggested it can produce NTC, we believe their figures show near perpendicular beaming.

6 Conclusion

When the Earth's radial vector lay within ±15° of the Van Allen Probes spin plane (in the dawn sector), spin modulation curve fits were made to the 0.5 s cadence HFR frequency-time spectra data. These fits were performed at all f over the entire mission while in the dawn sector, which covers a vast range of plasmapause locations. To select nonthermal continuum radiation NTC, frequency-time pixels where selected using the following criteria: the frequency f was greater than 1.2 f_{pe}, the modulation index m was greater than 0.6, the relative error in m was small, and the ratio of the χ^2/χ_0^2 a sine wave to a constant offset fit was small. A m of 0.6 was chosen to ensure that the wave vector $\boldsymbol{k}$ lies with ~30° of the spin plane, given the limitation on the interpretation of m. The beaming angle Θ_B was estimated as the angle between the wave vector direction in the spin plane and the Z_{SM} axis.

449 Below 100 kHz, for a given f and radial distance bin, the observed pattern of θ_B versus
450 magnetic latitude λ_M forms an inverted pattern with the apex at the SM magnetic equator. Using
451 the NTC beaming formula from LMCT, we show that such a pattern is predicted due to the large
452 radial variation of the source equatorial plasmapause. Quantitatively the θ_B has a systematic shift
453 above the theory curve near that magnetic equator. A back of the envelope computation was
454 performed to show that if the plasmapause is not azimuthally symmetric at the window one
455 expects a systematic offset of 5-10° toward larger θ_B. We discuss several factors that make the
456 use of m in estimating of the out of spin plane component difficult. Two of the factors are
457 smoothing of data before fitting and variation in the Z-mode intensity at the radio window over
458 the fit interval. By taking attenuation into account (Budden, 1980), we showed that the model
459 inverted V becomes broadened in beaming angle by of about 10° near the window center (Figure
460 9d) at -20 db. This suggests that attenuation could be the major factor contributing to the spread
461 in beaming angle. These factors make achievement of quantitative agreement between
462 observations and theory difficult, if not impossible.
463
464 We found (for $1 \leq K_p \leq 4$) a negative Spearman correlation coefficient for the 3
465 frequencies investigated below 100 kHz, one with a weak correlation value and two with
466 moderate values. This trend is expected, because as K_p index decreases the plasmapause on
467 average will move outwards and f_{ce} will decrease leading to a decrease θ_B from theory. We
468 conclude that these two observations, 1) the observed inverted V pattern of θ_B vs λ_M and 2) the
469 weak to moderate K_p dependence, highly suggest that LMCT is the dominant mechanism for the
470 generation of NCT for $f < 100$ kHz.
471

For f >100 kHz, our selections become contaminated with L-O mode AKR, this contamination decreases for $|\lambda_M|$ (< 10°). A partial inverted V is observed at the low end of this f range, and no reliable trend in K_p index is observed. Unlike emissions with f < 100 kHz, where the clustering of detections tends to lie off the magnetic equator consistent with beaming out the equatorial plane, these emissions are clustered around the magnetic equator. We conclude that LMCT can explain only a subset of these observations for f> 100 kHz and that another mechanism is also needed in this f range.

Acknowledgments

We acknowledge fruitful discussions and comments from Dr. William S. Kurth. The work for the study was funded by NASA Roses Grant 80HQTR18T0066. This work was also partly funded by NASA through the GPHI Cooperative Agreement NNG11PL02A and PHASER 80NSSC21M0180. This material is based upon work supported by the U.S. Department of Energy, Office of Science, Office of Fusion Energy Sciences under contract DE-AC02-09CH11466. Work at Princeton University is under National Aeronautics and Space Administration (NASA) Grants 80HQTR18T0066 and 80HQTR19T0076. Work at Andrews University is supported by NASA grants NNX16AQ87G, 80NSSC19K0270, 80NSSC19K0843, 80NSSC18K0835, 80NSSC20K0355, NNX17AI50G, 80HQTR18T0066, 80NSSC20K0704, 80NSSC18K1578, 80NSSC22K0515, and NSF grants AGS1832207, AGS1602855, and AGS2131013.

Data Availability Statement

494 For attitude calculations, the NAIF ICY toolkit was used, the ephemeris data required by the
495 toolkit is at https://cdaweb.gsfc.nasa.gov/pub/data/rbsp/rbspa/ephemeris/. The dataset citation for
496 the HFR spectral data is Kletzing, C. A. (2022a), for plasma density is Kurth et al. (2022), and
497 the K_p index is Papitashvili and King, (2020). These datasets are available at the
498 https://cdaweb.gsfc.nasa.gov.
499
500
501 **References**
502 Acton, C.H., "Ancillary Data Services of NASA's Navigation and Ancillary Information
503 Facility;" Planetary and Space Science (1996), Vol. 44, No. 1, pp. 65-70;
504 DOI 10.1016/0032-0633(95)00107-7
505
506 Acton, C., N. Bachman, B. Semenov, Edward Wright (2017), A look toward the future in the
507 handling of space science mission geometry; Planetary and Space Science; DOI
508 10.1016/j.pss.2017.02.013
509
510 Bevington, P.R. & Robinson, D. 1992, *Data Reduction and Error Analysis for the Physical*
511 *Sciences* (WCB/McGraw-Hill).
512
513 Boardsen, S. A., J. L. Green, and B.W. Reinisch (2008), Comparison of kilometric continuum
514 latitudinal radiation patterns with linear mode conversion theory, *J. Geophys. Res.*, 113,
515 A01,219, doi: 10.1029/2007JA012319.
516

Budden, K.G (1980), The theory of radio windows in the ionosphere and magnetosphere, *Journal of Atmospheric and Terrestrial Physics*, 42-3, https://doi.org/10.1016/0021-9169(80)90036-7

Carpenter, D. L., & Anderson, R. R. (1992). An ISEE/Whistler model of equatorial electron density in the magnetosphere. *Journal of Geophysical Research*, **97**(A2), 1097– 1108. https://doi.org/10.1029/91ja01548

Cheng, C. -Z. (1975) Ordinary electromagnetic mode instability, Journal of Plasma Physics, 13, pp 335-348, doi 10.1017/S002237780002609X

Fainberg, J. (1979), Technique to determine location of radio sources from measurements taken on spinning spacecraft , NASA Technical Memorandum 80598. https://ntrs.nasa.gov/citations/19800008000

Farrell, W. M. (2001), Direct generation of O-mode emission in a dense, warm plasma: Applications to interplanetary type II emissions and others in its class, *J. Geophys. Res.*, 106(A8), 15701– 15709, doi:10.1029/2000JA000156.

Gough, M. P., Christiansen, P., Martelli, G. & Gershumy, E. J. (1979) Interaction of electrostatic waves with warm electrons at the geomagnetic equator. *Nature* **279,** 515–517, doi:10.1038/279515a0

Gough, M.P. (1982) Non-thermal continuum emissions associated with electron injections: Remote plasmapause sounding, *Planetary and Space Science* **30** (7), 657-668, doi: https://doi.org/10.1016/0032-0633(82)90026-5.

Grimald, S., Décréau, P. M. E., Canu, P., Suraud, X., Vallières, X., Darrouzet, F., and Harvey, C. C. (2007), A quantitative test of Jones NTC beaming theory using CLUSTER constellation, Ann. Geophys., 25, 823–831, doi: 10.5194/angeo-25-823-2007.

Gurnett, D. A. (1975), The Earth as a radio source: The nonthermal continuum, *J. Geophys. Res.*, 80(19), 2751– 2763, doi:10.1029/JA080i019p02751.

Gurnett, D. A., and Green, J. L. (1978), On the polarization and origin of auroral kilometric radiation, *J. Geophys. Res.*, 83(A2), 689– 696, doi:10.1029/JA083iA02p00689.

Gurnett, D. A., and Frank, L. A. (1976), Continuum radiation associated with low-energy electrons in the outer radiation zone, *J. Geophys. Res.*, 81(22), 3875– 3885, doi:10.1029/JA081i022p03875.

Gurnett, D. A., and Shaw, R. R. (1973), Electromagnetic radiation trapped in the magnetosphere above the plasma frequency, *J. Geophys. Res.*, 78(34), 8136– 8149, doi:10.1029/JA078i034p08136.

562 Green, J. L., Gurnett, D. A., and Shawhan, S. D. (1977), The angular distribution of auroral
563 kilometric radiation, *J. Geophys. Res.*, 82(13), 1825– 1838, doi:10.1029/JA082i013p01825.
564
565 Green, J. L., B. Sandel, S. Fung, D. Gallagher, and B. Reinisch (2002), On the origin of
566 kilometric continuum, *J. Geophys. Res.*, 107, doi: 10.1029/2001JA000,193.
567
568 Green, J. L., Boardsen, S., Fung, S. F., Matsumoto, H., Hashimoto, K., Anderson, R. R., Sandel,
569 B. R., and Reinisch, B. W. (2004), Association of kilometric continuum radiation with
570 plasmaspheric structures, *J. Geophys. Res.*, 109, A03203, doi:10.1029/2003JA010093.
571
572 Hashimoto, K., Calvert, W., and Matsumoto, H. (1999), Kilometric continuum detected by
573 Geotail, *J. Geophys. Res.*, 104(A12), 28645– 28656, doi:10.1029/1999JA900365.
574
575 Hashimoto, K., Anderson, R. R., Green, J. L., and Matsumoto, H. (2005), Source and
576 propagation characteristics of kilometric continuum observed with multiple satellites, *J.*
577 *Geophys. Res.*, 110, A09229, doi:10.1029/2004JA010729.
578
579 Horky, M. and Y. Omura (2019), Novel nonlinear mechanism of the generation of non-thermal
580 continuum radiation, Physics of Plasmas **26**, 022904 (2019); https://doi.org/10.1063/1.5077094
581
582 Horne, R. B. (1989), Path-integrated growth of electrostatic waves: The generation of terrestrial
583 myriametric radiation, *J. Geophys. Res.*, 94(A7), 8895– 8909, doi:10.1029/JA094iA07p08895.
584

585 Jones, D. (1976), Source of terrestrial non-thermal radiation *Nature* **260,** 686–689,
586 https://doi.org/10.1038/260686a0
587
588 Jones, D. (1980), Latitudinal beaming of planetary radio emissions. *Nature* **288**, 225–229.
589 https://doi.org/10.1038/288225a0
590
591 Jones, D., Calvert, W., Gurnett, D. A., & Huff, R. L. (1987), Observed beaming of terrestrial
592 myriametric radiation. *Nature* **328,** 391–395. https://doi.org/10.1038/328391a0
593
594 Kletzing, C. A., et al. (2013), The Electric and Magnetic Field Instrument Suite and Integrated
595 Science (EMFISIS) on RBSP, *Space Sci. Rev.*, 179, 127–181, doi:10.1007/s11214-013-9993-6.
596
597 Kletzing, C. A. (2022), Van Allen Probe A Single Axis AC Electric Field Spectra burst data
598 [Data set]. NASA Space Physics Data Facility. https://doi.org/10.48322/18b2-kt74.
599
600 Kurth, W.S. (1982), Detailed observations of the source of terrestrial narrowband
601 electromagnetic radiation. Geophys. Res. Lett., 9: 1341-1344.
602 https://doi.org/10.1029/GL009i012p01341
603
604 Kurth, W. S., Baumback, M. M., and Gurnett, D. A. (1975), Direction-finding measurements of
605 auroral kilometric radiation, *J. Geophys. Res.*, 80(19), 2764– 2770,
606 doi:10.1029/JA080i019p02764.
607

608 Kurth, W.S., Frank, L.A., Ashour-Abdalla, M., Gurnett, D.A. and Burek, B.G. (1980),
609 Observations of a free-energy source for intense electrostatic waves. Geophys. Res. Lett., 7: 293-
610 296. https://doi.org/10.1029/GL007i005p00293
611
612 Kurth, W. S., Gurnett, D. A., and Anderson, R. R. (1981), Escaping nonthermal continuum
613 radiation, *J. Geophys. Res.*, 86(A7), 5519– 5531, doi:10.1029/JA086iA07p05519.
614
615 Kurth, W. S., De Pascuale, S., Faden, J. B., Kletzing, C. A., Hospodarsky, G. B., Thaller, S. and
616 Wygant, J. R. (2015), Electron densities inferred from plasma wave spectra obtained by the
617 Waves instrument on Van Allen Probes. *J. Geophys. Res. Space Physics*, 120: 904– 914. doi:
618 10.1002/2014JA020857.
619
620 Kurth, W. S., S. De Pascuale, J. B. Faden, C. A. Kletzing, G. B. Hospodarsky, S. Thaller, and J.
621 R. Wygant (2022). Van Allen Probe A Electric and Magnetic Field Instrument Suite and
622 Integrated Science (EMFISIS) Density and other Parameters derived by digitizing Traces on
623 Spectrograms, Level 4 (L4), 0.5 s Data [Data set]: RBSP-A_DENSITY_EMFISIS-L4. NASA
624 Space Physics Data Facility. https://doi.org/10.48322/c4ha-xj50.
625
626 Menietti, J. D., Gurnett, D. A., Kurth, W. S., Groene, J. B., and Granroth, L. J. (1998), Galileo
627 direction finding of Jovian radio emissions, *J. Geophys. Res.*, 103(E9), 20001– 20010,
628 doi:10.1029/97JE03555.
629

630 Moldwin, M. B., Downward, L., Rassoul, H. K., Amin, R., & Anderson, R. R. (2002). A new
631 model of the location of the plasmapause: CRRES results. *Journal of Geophysical Research*,
632 **107**(A11). SMP1-9–SMP2-9. https://doi.org/10.1029/2001ja009211
633
634 Morgan, D. D., and D. A. Gurnett (1991), The source location and beaming of terrestrial
635 continuum radiation, J. Geophy. Res., 96, 9595. https://doi.org/10.1029/91JA00314
636
637 Papitashvili, N. E., & and King, J. H. (2020), OMNI Hourly Data Set [Data set]. NASA Space
638 Physics Data Facility. **https://doi.org/10.48322/1shr-ht18**.
639
640 Rönnmark, K., Christiansen, P. Dayside electron cyclotron harmonic emissions.
641 *Nature* **294,** 335–338 (1981). https://doi.org/10.1038/294335a0
642
643 Sandel, B., Goldstein, J., Gallagher, D. *et al.* Extreme Ultraviolet Imager Observations of the
644 Structure and Dynamics of the Plasmasphere. *Space Science Reviews* **109,** 25–46 (2003).
645 https://doi.org/10.1023/B:SPAC.0000007511.47727.5b
646
647 Sentman, D.D., Frank, L.A., Gurnett, D.A., Kurth, W.S. and Kennel, C.F. (1979), Electron
648 distribution functions associated with electrostatic emissions in the dayside magnetosphere.
649 Geophys. Res. Lett., 6: 781-784. https://doi.org/10.1029/GL006i010p00781
650

651 Xiao, F., Zhou, Q., Su, Z., He, Z., Yang, C., Liu, S., He, Y., and Gao, Z. (2016), Explaining
652 occurrences of auroral kilometric radiation in Van Allen radiation belts, *Geophys. Res. Lett.*, 43,
653 11,971– 11,978, doi:10.1002/2016GL071728.

654

655

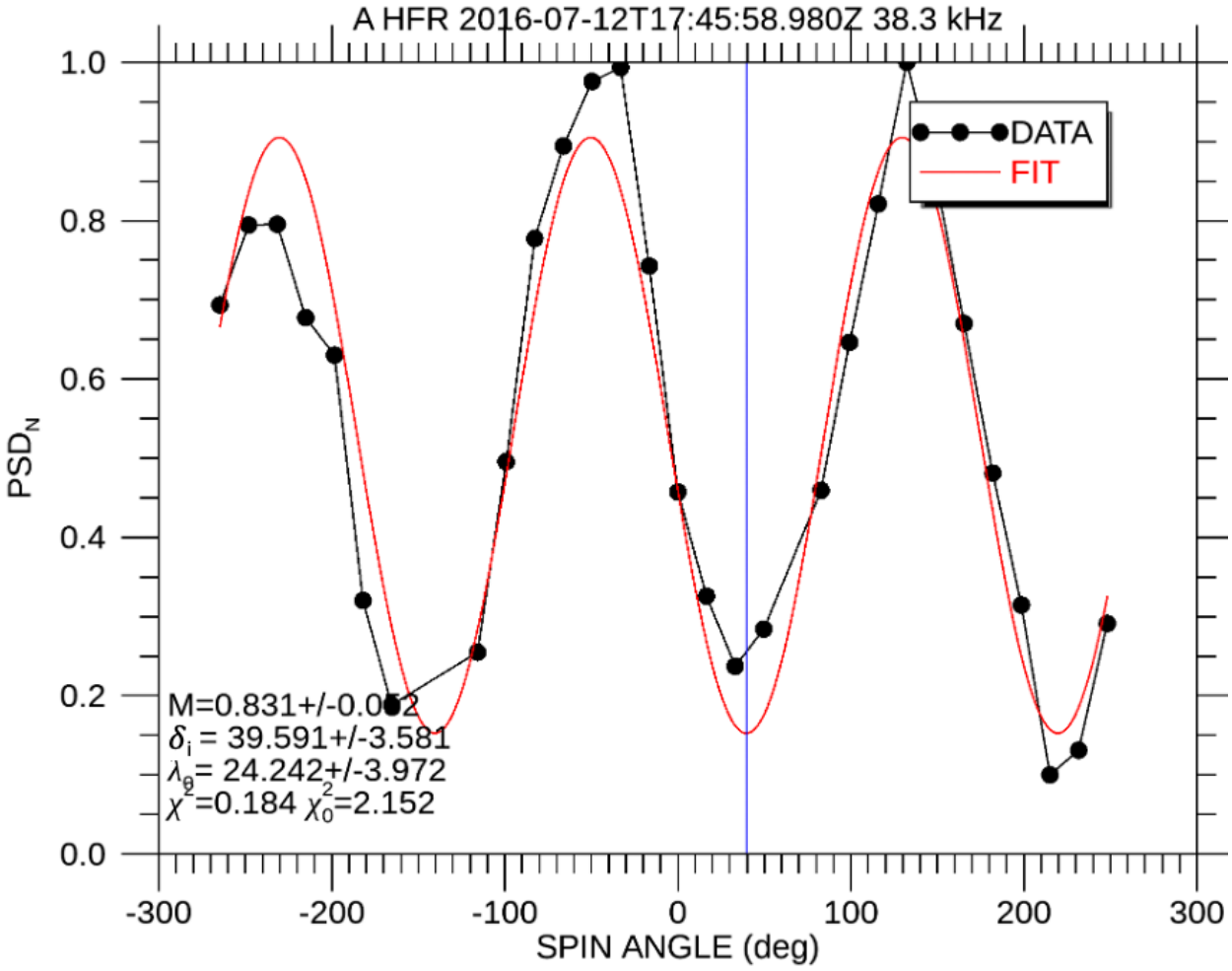

656

657 Figure 1. An example fit of the spin modulation curve for the frequency channel at 38.3 kHz.
658 The fit parameters and their uncertainties are listed. The power spectral density PSD_N is
659 normalized to the peak value. χ^2 is the chi squared of the spin modulation curve fit and χ^2_0 is the
660 chi squared for a constant offset fit.

661

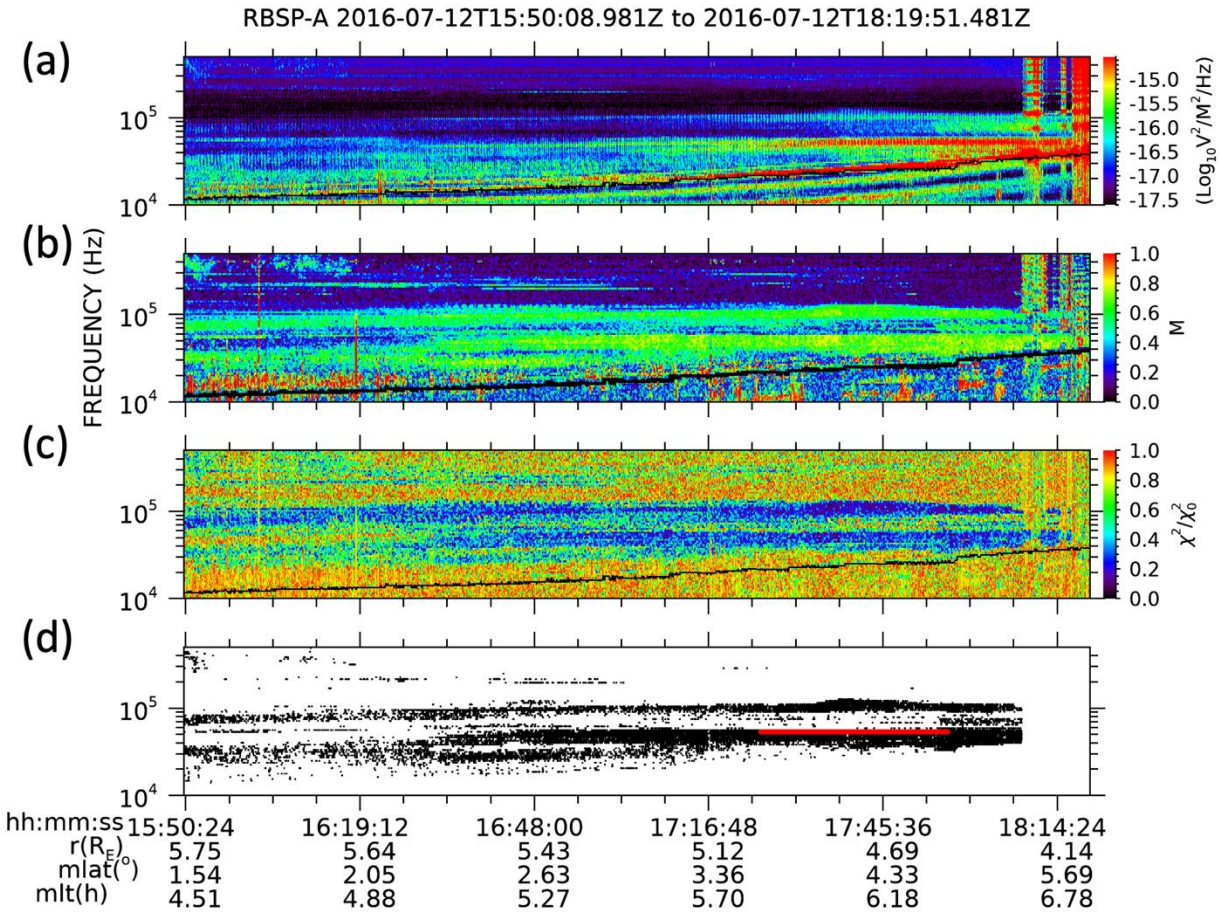

Figure 2. Escaping continuum example. Panel (a) spectrogram of the phase space density, (b) spectrogram of the modulation index *m*, (c) χ^2/χ^2_0 ratio, and (d) selections. The black line is the UHF derived plasma frequency. The red lines in panel (d) correspond to selections at 53.6 kHz between 4.5 and 5 R_E used in Figure 8, 9 & 10.

669

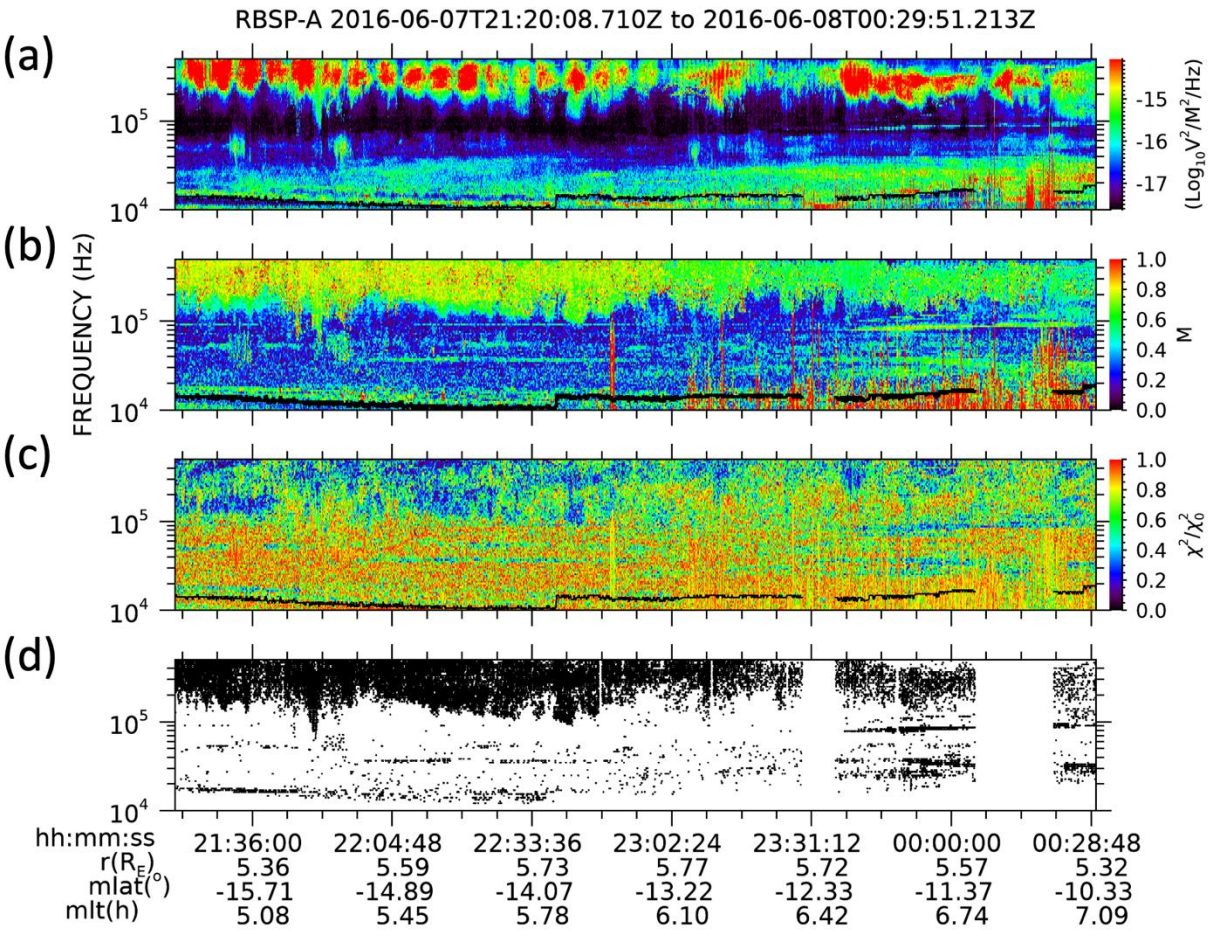

670

671 Figure 3. Emissions at *f* from 200 to 500 kHz are interpreted to be L-O mode AKR a source of
672 contamination of the selections above 100 kHz. Panel (a) spectrogram of the phase space density,
673 (b) spectrogram of the modulation index *m*, (c) χ^2/χ^2_0 ratio, and (d) selections. The black line is
674 the UHF derived plasma frequency.

675

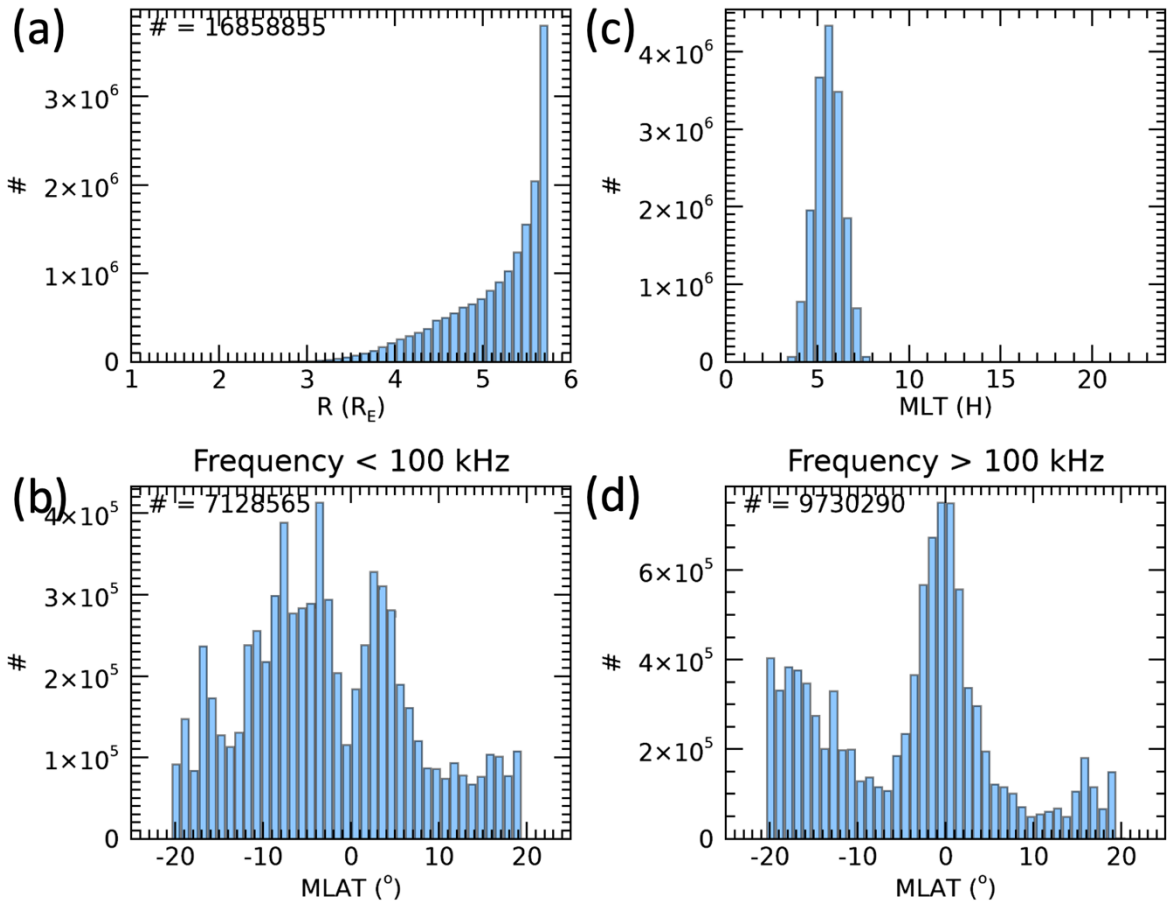

676

677 Figure 4. Histogram of the selections: (a) radial distance, (c) Magnetic local time, and magnetic

678 latitude for (b) $f < 100$ kHz and (d) $f > 100$ kHz.

679

680

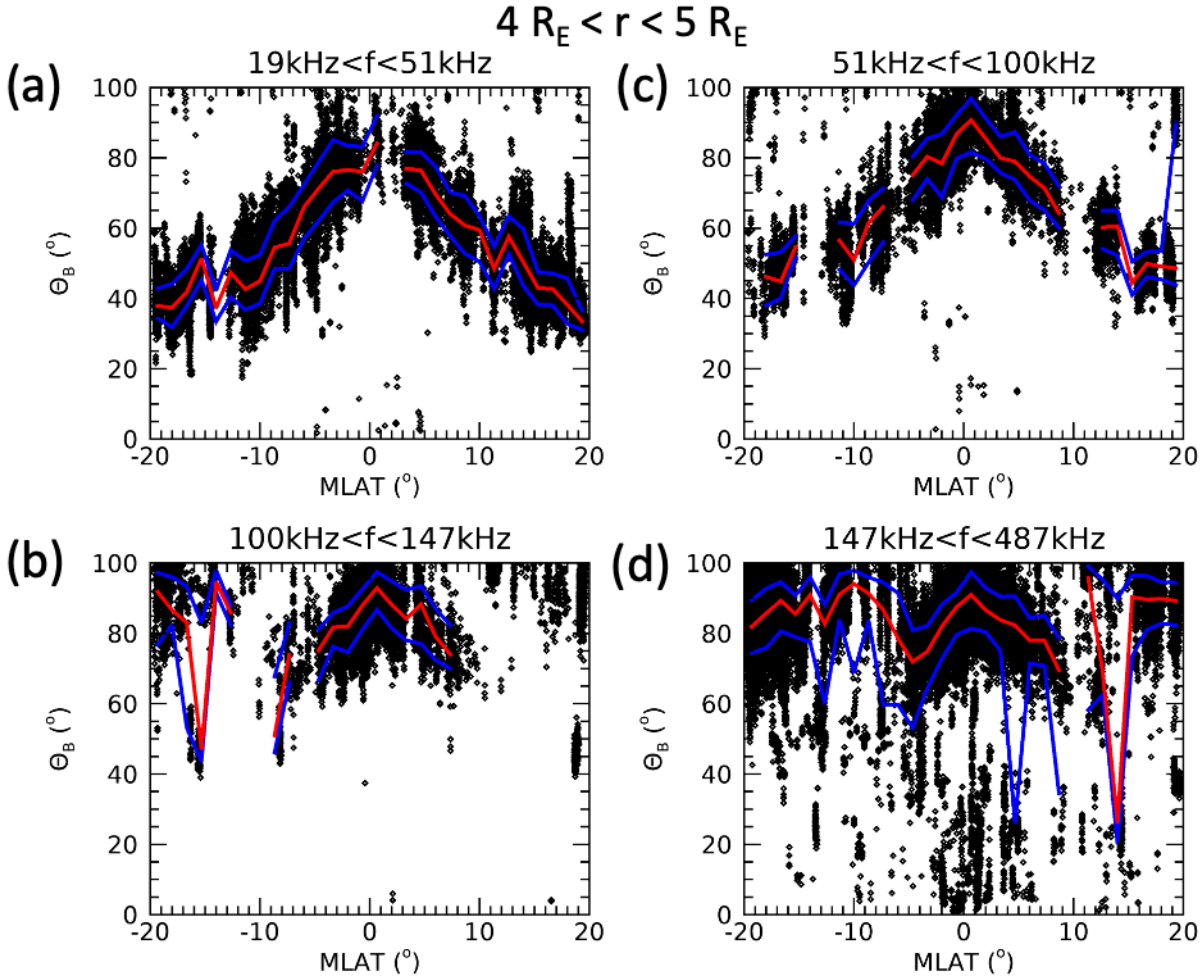

681

682 Figure 5. Scatter plots for 4 R_E < r < 5 R_E of beaming angle θ_B versus magnetic latitude. For (a) f

683 <50 kHz, (b) 50kHz < f < 100kHz, (c) 100kHz < f < 150kHz , and (d) 150kHz < f < 500kHz. The

684 curves are the running percentiles, blue 50th (median), red 16th and 84th percentiles.

685

686

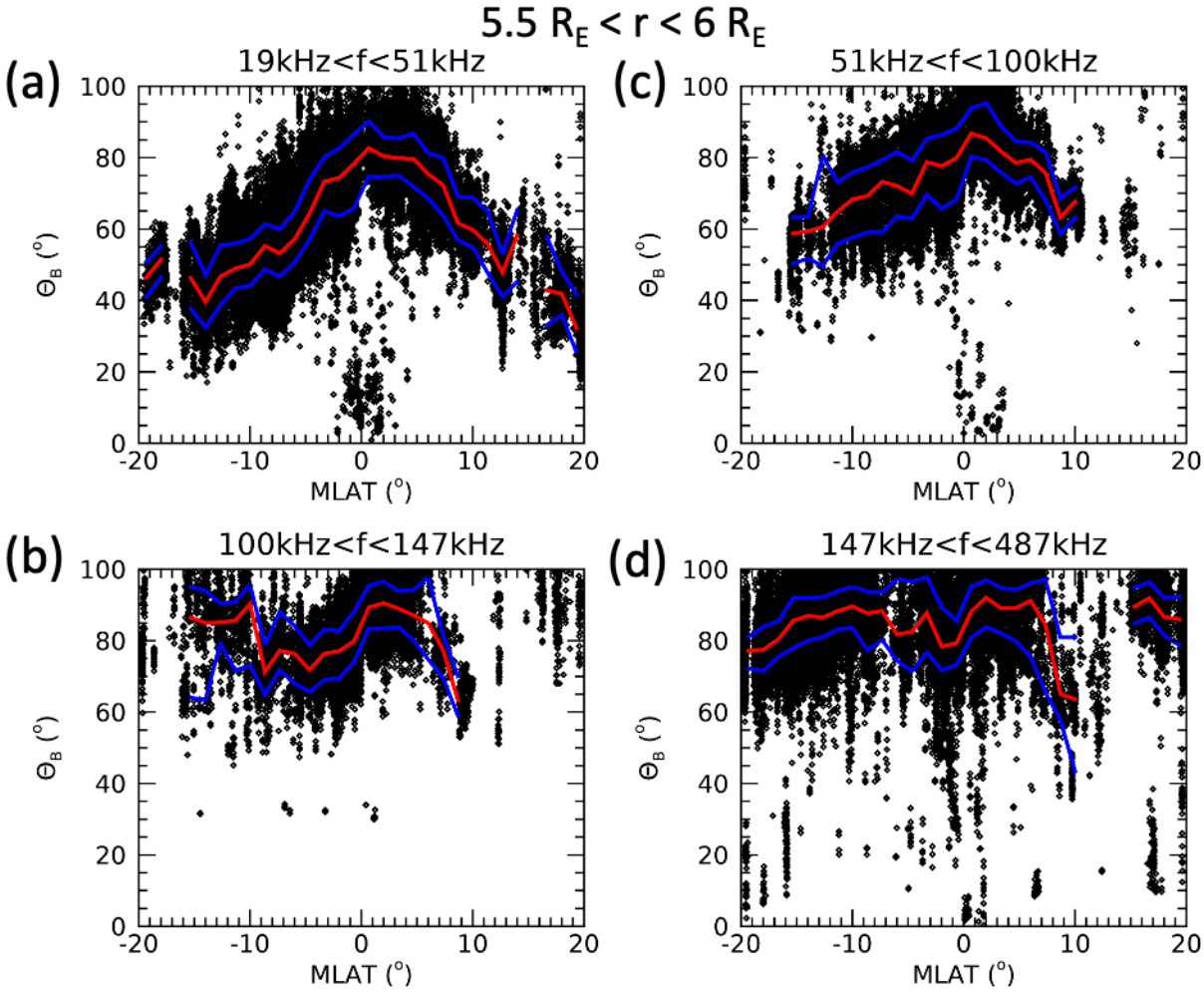

687

688 Figure 6. Scatter plots for r >5.5 R_E of beaming angle θ_B versus magnetic latitude. For (a) f <50

689 kHz, (b) 50kHz < f < 100kHz, (c) 100kHz < f < 150kHz , and (d) 150kHz < f < 500kHz. The

690 curves are the running percentiles, blue 50th (median), red 16th and 84th percentiles.

691

692

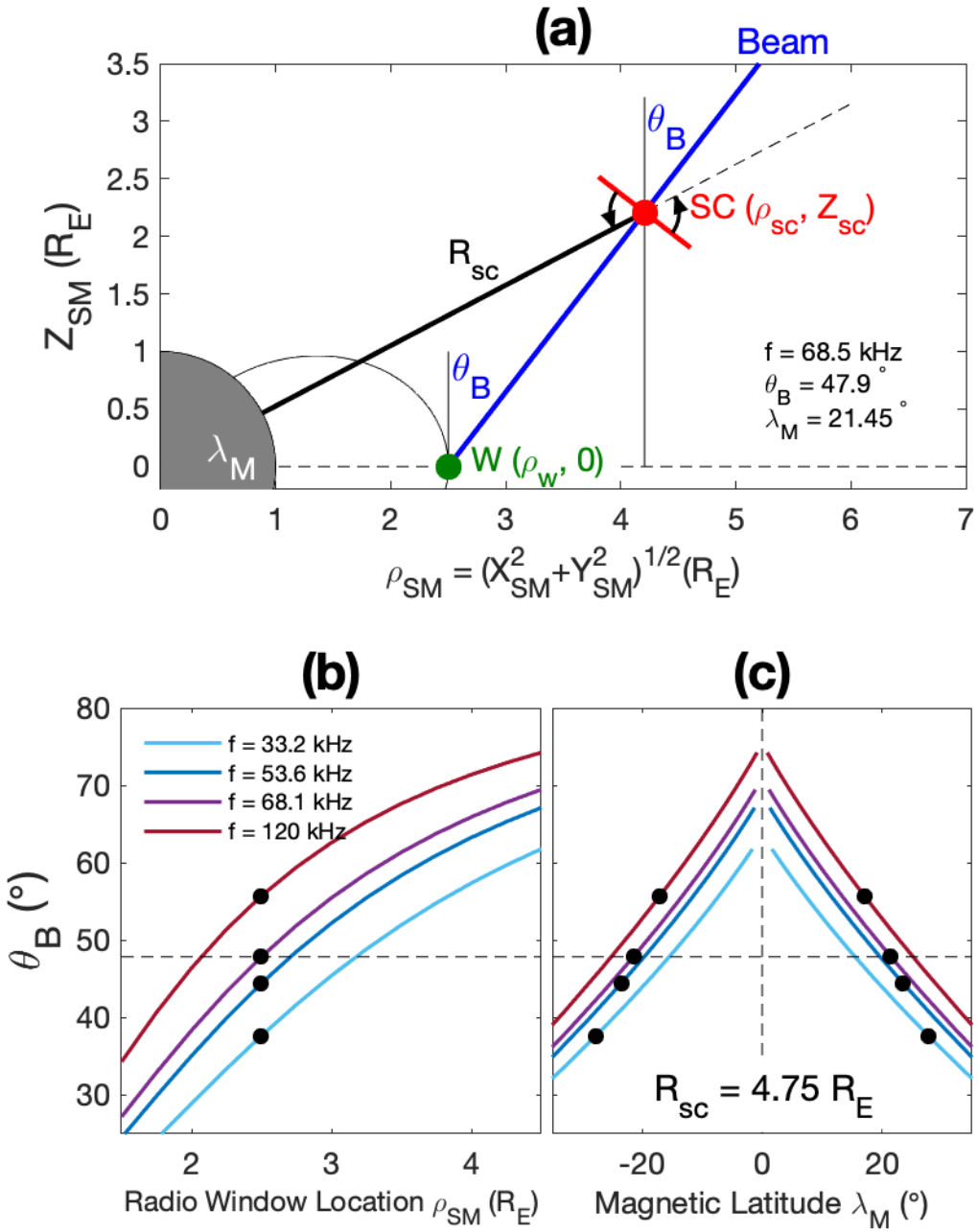

693

694 Figure 7 (a) Illustration of the meridian beaming geometry. The blue line represents the NTC

695 beam emitted at the radio window *W* (green circle). The satellite *SC* (red circle) is at a radial

696 distance R_{SC} and magnetic latitude λ_M. Θ_B is measured from background magnetic field ***B*** (***B*** ||

697 $\mathbf{Z_{SM}}$) at *W*. (b) Θ_B as *W* changes with radial distance. Θ_B (black circles) when *W* is located at

698 L=2.5R_E (i.e., the plasmapause is at 2.5R_E). (c) The predicted Θ_B for R_{SC} at 4.75 R_E versus λ_M for

699 plasmapause locations varying between 1.5 to 4.75 R_E. For example, at f = 68.1 kHz emission
700 from a plasmapause located at 2.5R_E with a θ_B of 47.9° (b) will be observed by a spacecraft at
701 4.75R_E at λ_M of ±21.45°, indicated by the dashed horizontal line in panels (b) and (c).

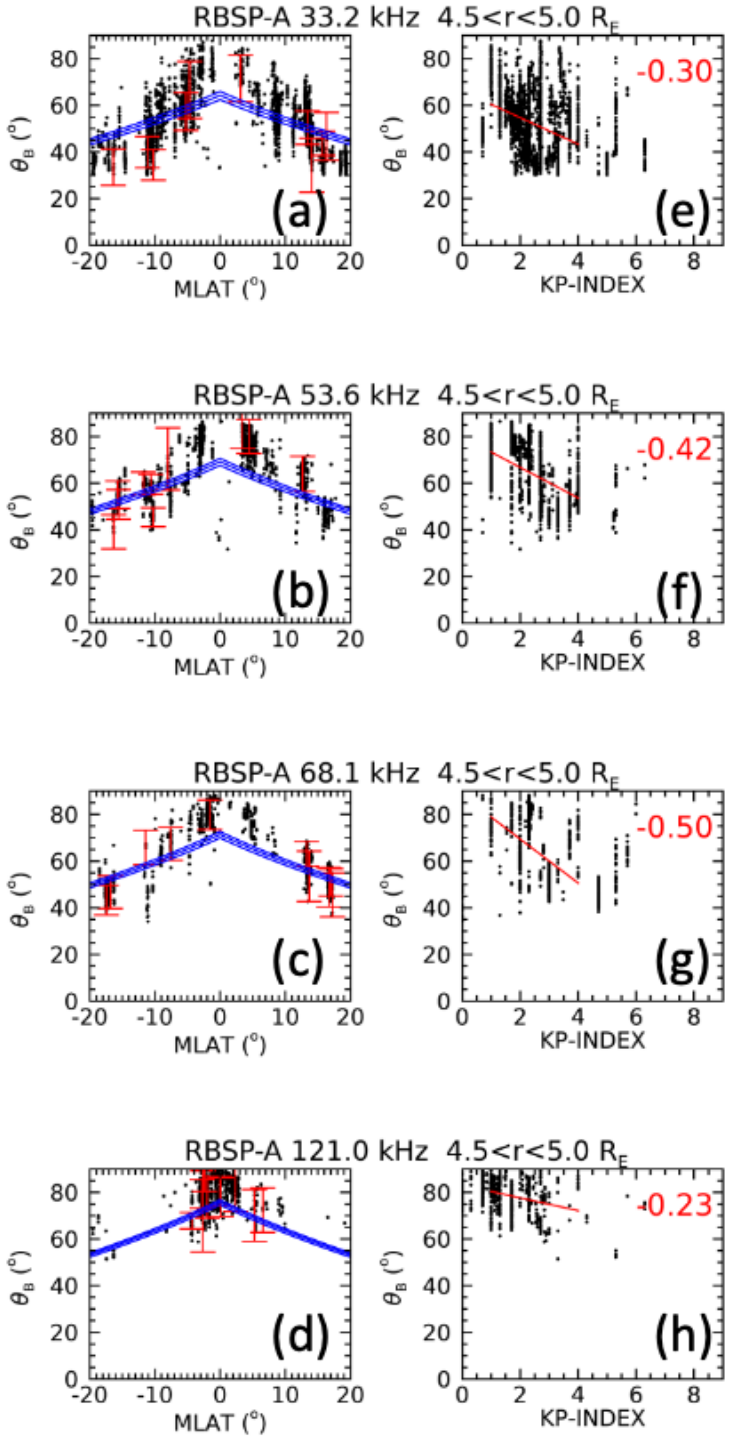

Figure 8. Scatter plots for r between 4.5 and 5.0 R_E; beaming angle (a-d) θ_B versus magnetic latitude and (e-i) K_p index, for frequencies of 33.2 kHz, 53.6 kHz, 68.1 kHz, and 121.0 kHz. The

706 blue curves (a-d) are the statistical LMCT theory curves for r of 4.5, 4.75, and 5.0 R_E. Error bars
707 indicated by red brackets are plotted for 10 randomly selected measurements. In (e-h) the red
708 lines are linear fits, and the red numbers are the non-linear Spearman correlation coefficients,
709 which lie in the (e) weak, (f) moderate, (g) moderate, and (h) poor range.
710

711

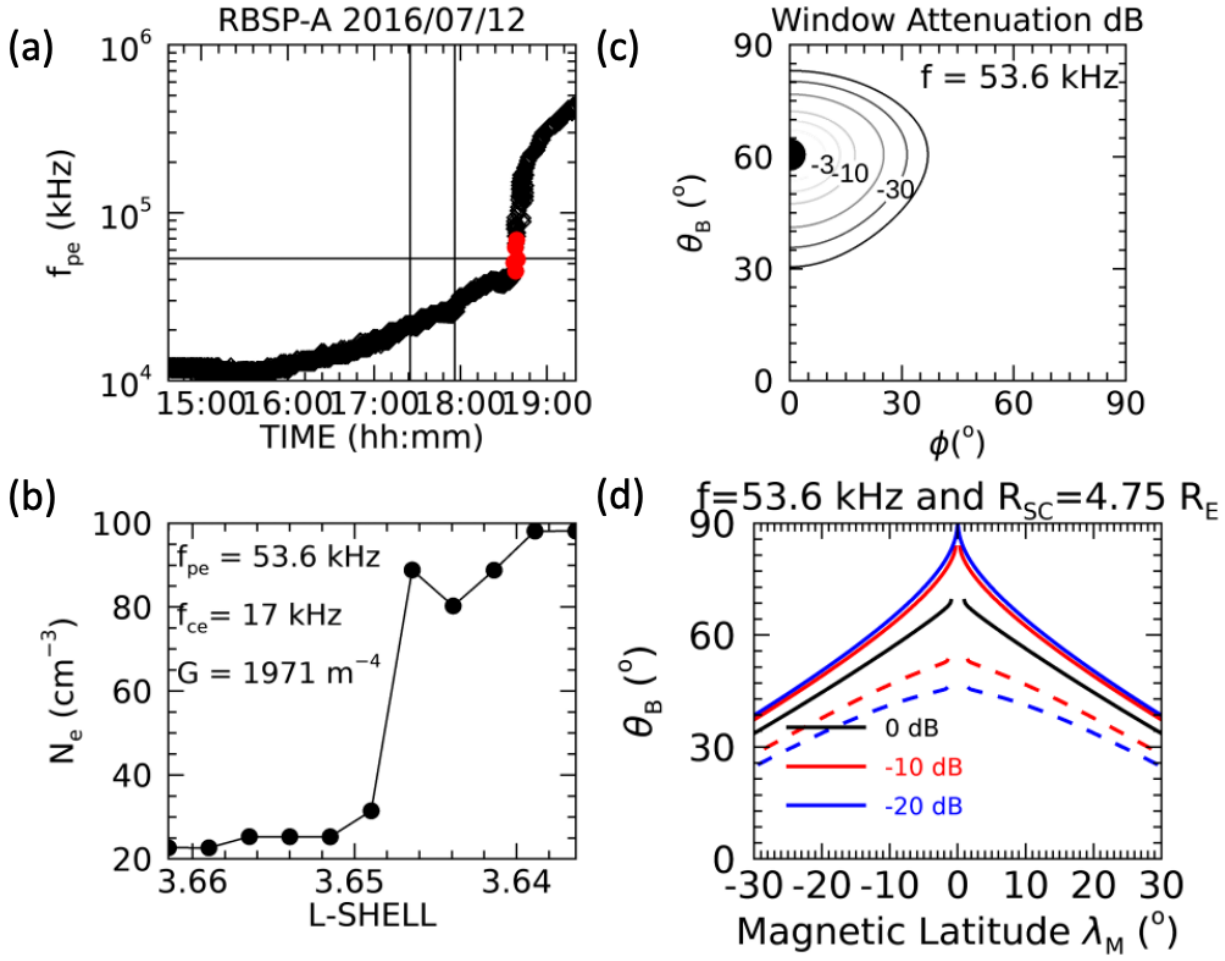

712

713 Figure 9 (a) The nearest plasmapause is indicated (red dots), where f = 53.6 kHz intersects f_{pe} for
714 the NTC emissions shown in Figure 2. The vertical lines are where the orbit goes from 5.0 to 4.5
715 RE. (b) The intersection point is at L=3.65, magnetic latitude = 7.18°, MLT=7 h, the radial
716 electron density gradient is G is -1971 m^{-4}. (b) For f=53.6 kHz the radio window attenuation in
717 decibels is shown as a function θ_B and ϕ (azimuthal angle measured from the plasmapause).
718 The window center is indicated by the black dot where the attenuation is 0 dB (100%
719 transmission). (c) The inverted V pattern is shown for f = 53.6 kHz using same assumptions as in
720 Figure 7, but attenuation of emissions that are off centered are included. Black curve is at the

721 window center, same as that of Figure 7, the red (blue) curves are for emissions attenuated by -
722 10 dB (-20 dB).
723

724

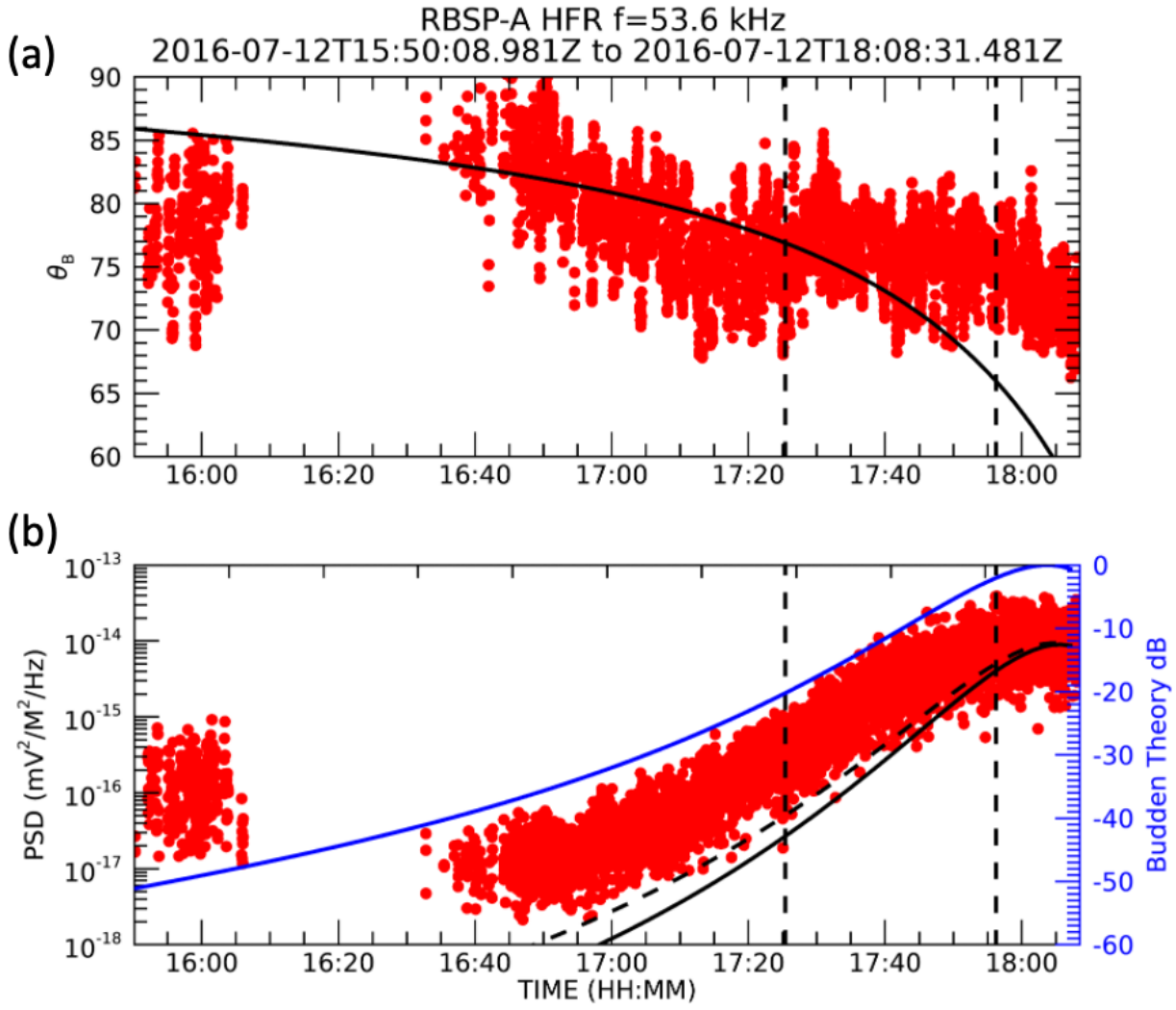

725

726 Figure 10. At a frequency of 53.6 kHz for the orbit segment shown in Figure 2 a scatter plot (red
727 circles) is shown of (a) signal measured θ_B and (b) Power Spectral Density versus time. The
728 black curve in (a) is θ_B based on the spacecraft location and the estimated window location, and
729 the blue curve for (b) is the attenuation of the signal in decibels given by equation (23) of
730 Budden (1980) (right y-axis) for the curve in (a). The dashed and dotted lines are the PSD
731 proportional to the power of the attenuation times $1/\rho_w^2$ and $1/\rho_w$ respectively. The two vertical
732 dashed lines are where the orbit goes from 5.0 to 4.5 REcs.

733

734